IEEE Access
Multidisciplinary ⋮ Rapid Review ⋮ Open Access Journal

Received November 8, 2019, accepted December 13, 2019, date of publication December 17, 2019,
date of current version December 30, 2019.

Digital Object Identifier 10.1109/ACCESS.2019.2960387

Hybrid Cardiac Imaging Integrating Elliptical Orbit SPECT With CT

JINHUA SHENG, (Senior Member, IEEE), YANGJIE MA,
WEIXIANG LIU, AND QINGQIANG LIU
[1]College of Computer Science, Hangzhou Dianzi University, Hangzhou 310018, China
[2]Key Laboratory of Intelligent Image Analysis for Sensory and Cognitive Health, Ministry of Industry and Information Technology of China,
Hangzhou 310018, China

Corresponding author: Jinhua Sheng (jsheng@hdu.edu.cn)

This work was supported by the National Natural Science Foundation of China (NSFC) under Grant 61871168.

ABSTRACT The cardiac single photon emission computed tomography (SPECT) is an important research topic because of the large clinical demand and the need for improving image quality. It usually suffers from low count sensitivity and poor spatial resolution due to patient radiation safety concerns. In this study, hybrid cardiac imaging integrating elliptical orbit SPECT (E-SPECT) with computed tomography (CT) is proposed to better obtain the anatomical and physiological information of the cardiac and vascular systems. The geometric structure of this proposed hybrid imaging system is similar to that of an ellipse, containing multiple detectors with slit-slat collimation. The hybrid imaging system utilizes the elliptical geometry and multi-detectors to improve the sensitivity and signal to noise ratio (SNR), and incorporates a CT scanner into the system to obtain an accurate attenuation mapping matrix of the patient for image reconstruction. The iterative reconstruction algorithm with some constraints is used to reconstruct images. The constraint-based body contour is introduced to deal with severely truncated data from E-SPECT. The feasibility and advantage of the system is validated by simulations. Simulation results show that it is optimal for system design and the quality of reconstructed images are greatly improved. With an optimal sampling coverage angle between 210° and 240°, the hybrid cardiac imaging system proposed in the paper can achieves significant improvements in image spatial resolution, SNR and image fidelity.

INDEX TERMS Attenuation correction (AC), computed tomography (CT), elliptical orbit, ordered subsets expectation maximization (OSEM), single photon emission computed tomography (SPECT), slit-slat collimation.

I. INTRODUCTION

Nuclear medicine has advanced to be a clinical and research discipline for assessing the function of normal and diseased tissues [1]. It can help doctors obtain structural and functional information about the tissue inside the human body. Single photon emission computed tomography (SPECT) and positron emission tomography (PET) are considered as imaging techniques best suited to investigate organ function [2]. PET is superior to SPECT in terms of imaging quality and the effect of localizing the lesion. However PET has a big drawback that it can use very few tracers, which limits the application of PET in different fields. The radionuclide used in SPECT has a longer physical half-life than PET radionuclides, and its half-life is more consistent with the physiological processes in the region of interest of the body. Addition, the radionuclide used in SPECT can be easily made without using a medical cyclotron [3]. Because of these reasons, over three-quarters of clinical procedures of nuclear medicine use SPECT.

In the past decades, SPECT has played an indispensable role in clinical diagnosis and treatment, especially in the field of clinical diagnosis of heart disease [4]. However, the existing SPECT systems still have some limitations [5], such as low photoelectric signal conversion efficiency and low spatial resolution. A primary application of current SPECT research in cardiac field is drug development [6]. There is a safe threshold on the drug injection dose in order to avoid damage to the human heart. The major inherent limitations for SPECT imaging are poor detection efficiency of 3-5% of the

The associate editor coordinating the review of this manuscript and approving it for publication was Wen Chen.

FIGURE 1. Photograph of CardiArc camera specifically is designed for cardiac imaging.

FIGURE 2. D-SPECT gantry and chair design.

injected dose low signal-to-noise (SNR) ratio and low spatial resolution.

Many solutions have been proposed in order to solve the above problems. CardiArc camera proposed by Patton, *et al.* [7] is a new design which rotates along the semicircular camera trajectory around the patient, as shown in Fig. 1. D-SPECT, proposed by Spectrum Dynamics (Haifa, Israel) [2], as shown in Fig.2, successfully solves the problem of low SNR and low photoelectric conversion efficiency, and the model has been successfully manufactured and marketed. However, these models still have shortcomings. The former has a relatively large constraint on the body shape, and the latter has insufficient scanning angle. And neither of them takes the attenuation map from the same machine, which will lead to the inaccuracy of the attenuation mapping matrix.

The attenuation map problem can be resolved by a combined SPECT/CT design [8]. The CT data was used for the SPECT attenuation correction. Since then, SPECT/CT was developed to detect metabolic pathologies and concomitant anatomical locations with significant therapeutic impact [9], [10]. In the paper, we propose a new hybrid cardiac imaging integrating elliptical orbit SPECT with CT, which offers more diagnostic values.

II. MATERIAL AND METHODS

Our goal is to detect emitted photons more effectively to improve the quality of SPECT system. We will use the combination of slits and slats to provide relatively higher count sensitivity [11]. It has been known that non-circular or elliptical orbit of rotation can result in improved spatial resolution and uniformity for SPECT imaging [12]. Here we attempt to develop a hybrid cardiac imaging system integrating elliptical orbit SPECT (E-SPECT) with CT with high count sensitivity, reasonably high temporal and spatial resolution.

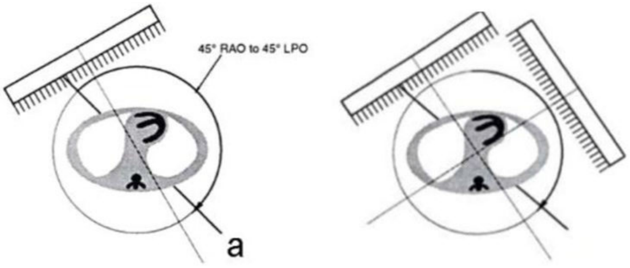

a) standard single detector b) two detectors

FIGURE 3. SPECT camera configuration; a): standard single detector camera the counts can be collected in the 180° between 45° RAO (right anterior oblique) and 45° LPO (left posterior oblique); b): two detectors double the sensitivity for 360° orbits.

A. CONVENTIONAL MODELS

The scanning device used in the conventional SPECT is the scintillation Angle camera. Each camera contains a parallel-hole collimator, and behind the collimator there is a set of NaI (TI) scintillation crystals connected to a photomultiplier tube. The scanning device of the system is mainly composed of 1 or 2 Angle cameras, as shown in Fig. 3. The working process of the system is that the Angle camera rotates around the human body and stops at a certain angle to receive the photons emitted from the human body. Intuitively the time for scanning photons emitted by the human body can be reduced by doubling the number of Angle camera. However, due to the limitation of the geometric structure of the system, it is impossible to add multiple angle cameras in a small range.

In the conventional model, in order to avoid the Angle camera colliding with the human body in the process of rotation, the distance between the Angle camera and the human body needs to be large. That leads to low SNR because the greater the distance between people and cameras is, the lower the signal detected. In addition, the conventional model has a longer scanning time due to the limitation of the number of cameras.

B. NEW CARDIAC IMAGING SYSTEM

Improvements in hardware and software have enabled the integration of dual imaging modalities. At the component level there are improvements in scintillators and photon transductors, as well as semiconductor detectors. The new scanning device we propose is an E-SPECT for cardiac with high count sensitivity, which does not use conventional collimation. It is combined with a CT to form the hybrid SPECT/CT. We also propose new reconstruction algorithms and image processing methods for this novel cardiac imaging system.

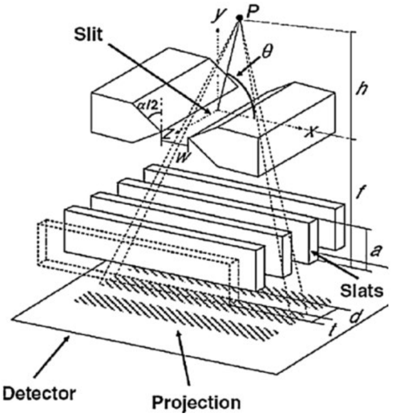

FIGURE 4. Perspective conceptual drawing of slit–slat collimator.

1) DETECTION AND COLLIMATION DEVICES

Collimator is an indispensable part of all SPECT models, and the main function of the collimator is to allow γ-rays in a certain angular range within a certain field of view to enter the detector through the aperture of the collimator, while the rays outside the field of view that do not conform to the angle of the collimator are shielded by the collimator. In that sense, collimator plays the role of a spatial positioning selector. Because the traditional parallel-hole collimator has a large space requirement and cannot be installed in limited space, the slit-slat collimator [13] is used here. The slit consists of a series of small holes in the middle of the lead sheet. The slat consists of a set of parallel plates behind the slit. The structure of the collimator is shown in Fig. 4.

Where in this diagram, x, y, z are the coordinate axes, P is the emission source, θ is the incidence angle, h is the distance from the emission source to slit, f is the focal length of the collimator, w is the width of slit, t, a and d are the width, height and gap of the slats septa, respectively.

The collimation uses a slit to collimate the transverse direction and a set of slates to collimate the axial direction. The slit allows high sensitivity and fine system resolution. The slats, which are normal to the axis of rotation, provide axial collimation, resulting in nearly independent axial slices and complete sampling for moving orbits. Slit-slat collimation is chosen for E-SPECT imaging.

The projection information required for SPECT is acquired by γ-ray detectors, and the quality of the projection depends on the properties of these detectors. Generally, scintillators absorb γ-ray or x-ray to convert the visible light into an electronic pulse. The persistence of the scintillation limits the counting rate capability of the detectors and low counting rate is a big problem with SPECT when conventional collimation is used. Previously used Angle cameras consist of NaI (TI) scintillator crystals connected to a group of photomultiplier tubes (PMTs). Photons can be detected from an array of PMTs covering the detector back surface with the low quantum conversion efficiency ($\sim$20%) at 140 keV. Classical Angle cameras have a lot of drawbacks such as the low energy resolution of NaI (TI) scintillation crystals and low intrinsic spatial resolution of about 4 mm.

FIGURE 5. The new CZT detector.

Recently, semiconductor detectors have been used to permit the fabrication of smaller and more compact system that can be customized for particular applications. Semiconductor detectors can provide direct conversion of absorbed γ-ray energy into an electronic signal. Because there is no need for an intermediate high gain amplification stage, semiconductor detectors are compact and can operate at low voltage. The precision of signal is better than that of scintillators, resulting in correspondingly better energy resolution. The energy resolution of semiconductor detectors is much higher than that of NaI (TI) crystals. Semiconductors need only 3 eV of energy to produce an electron hole pair, whereas NaI (TI) crystals need about 30 eV to produce a photon, and only about 30% of the photons can reach the photomultiplier tube to produce electrons [14].

Cadmium telluride (CdTe) and cadmium zinc telluride (CZT) are room temperature semiconductor detectors with similar properties and can be available as pixelated detector arrays with an intrinsic spatial resolution of 2.4 mm. The existing CdZnTe detectors are shown in Fig. 5. Another Semiconductor detector with very high intrinsic spatial resolution is the charge coupled device (CCD). CCDs are also used for directly detecting γ-ray with very low efficiency, but it can be used for energies below 30 keV. Semiconductor detectors instead of NaI (TI) scintillators can be chosen for the new SPECT imaging system.

2) ELLIPTICAL ORBIT CARDIAC IMAGING SYSTEM

In order to solve the above-mentioned problems in conventional SPECT, a new model is proposed here for detecting photons emitted by the human body. The geometry of the scanning device of this model is similar to that of an ellipse. The specific structure is shown in Fig.4. In this configuration, the detector is closer to the heart of the human body, which improves the signal-to-noise ratio. If the patient's body is very large, the patient can adjust the body direction to become perpendicular to the direction shown in Fig. 6(b), in which case it can accommodate a larger body.

In the model shown in Fig.6, slits are located in an elliptical orbit with a long axis radius of 240 mm and a short axis radius of 168 mm. The slit is a small aperture with a radius of 2.5 mm

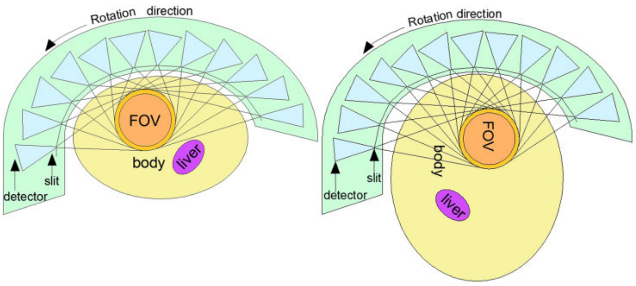

a) E-SPECT imaging system. b) E-SPECT for larger body size.

FIGURE 6. **a) Shows E-SPECT imaging in the form of part of an ellipse with multiple collimated detector columns; b) shows adjusting body orientation to fit patients with larger body size.**

TABLE 1. **System configuration parameters.**

No	w(mm)	d(mm)	t(mm)	f(mm)	a(mm)	α(°)
1	2.18	2.11	0.1	270	263	33
2	2.18	2.11	0.1	255	244	36
3	2.25	2.1	0.1	222	211	41
4	2.3	2.18	0.1	203	198	46
5	2.3	2.2	0.1	180	172	51
6	2.45	2.25	0.1	161	155	56
7	2.45	2.25	0.1	150	145	62
8	2.45	2.25	0.1	155	150	60
9	2.4	2.2	0.1	175	168	55
10	2.35	2.18	0.1	188	183	49
11	2.3	2.18	0.1	210	205	44
12	2.25	2.1	0.1	222	211	38

that allows photon to pass through, and be received by the detector. The big solid ellipse (long axis radius 200 mm, short axis radius 140 mm) in front of the orbit represents the cross-section of the body of a typical patient. The FOV with radius 70 mm is the region of the heart and the purple region is the liver. There are 12 slit-slat collimators in the whole elliptical orbit, and detectors are placed behind them to receive photons. With multiple detectors, sufficient reconstruction data can be collected with only a limited number of rotations to meet the basic coverage angle required for imaging. Therefore, the rotation time of this model will be much shorter than that of the classical model shown which uses only one or two detectors. Therefore, the new system is faster than classical model in obtaining data. It can be assumed that the intensity of γ-rays emitted by human body does not change during the data collection process. In data acquisition, the slit will rotate along its semielliptical orbit by 3° each time. A total of 15° need to be rotated, resulting in a total of 72 projection data sets (12×6). With these projection data, the heart image inside the human body can be obtained by appropriate local reconstruction algorithms.

The transaxial resolution for slit-slat is consistent with the pinhole resolution formula [15]:

$$R_0(transaxial) = R_0(pinhole) = \sqrt{R_g^2(pinhole) + (\frac{h}{f}R_i)^2}$$
$$= \sqrt{w2\frac{(h+f)^2}{f^2} + (\frac{h}{f}R_i)^2} \qquad (1)$$

Axial resolution can be shown experimentally to be consistent with the parallel-beam resolution formula [15]:

$$R_0(axial) = R_0(parallel) = \sqrt{R_g^2(parallel) + R_i^2}$$
$$= \sqrt{d^2\frac{(f+h)^2}{f^2} + R_i^2} \qquad (2)$$

In formulae (1) and (2), R_0 represents the resolution, R_g denotes the resolution of the collimator and R_i represents the inherent resolution of the detector. The parameters of the system are designed according to the formula mentioned above, shown in table 1.

In this model, the sensitivity of the system is determined by the width of slit and slat spacing. Once they are determined, the geometric efficiency of the system can be calculated by Eq.3 [16].

$$g(slit - slat)$$
$$= g(pinhole|parallel) = \sqrt{g(pinhole) \times g(parallel)}$$
$$= \sqrt{\frac{w^2}{4\pi h^2}\sin^3(\theta) \times \frac{d^4}{4\pi a^2 h(d+t)^2}\sin^3(\theta)} = \frac{wd^2}{4\pi ah(d+t)}\sin^3(\theta) \qquad (3)$$

Compared with the traditional system with only one angle camera, E-SPECT has a significant improvement in scanning time, which is less than one tenth of the traditional. The geometric efficiency of this system is 5.7×10^{-5} and the geometric efficiency of conventional SPECT is 2.30×10^{-5}. E-SPECT has two times improvement in spatial resolution for the central region compared with the traditional SPECT system. It is necessary to select a suitable detector for further improvement. E-SPECT replaced NaI (TI) crystals with CdZnTe semiconductors [17]. The CdZnTe can work normally at room temperature, and its volume is relatively small. The spatial resolution of the recent CdZnTe detector is about 2.5mm. In this model, detectors made of CdZnTe semiconductors are used with further improvement in spatial resolution.

3) HYBRID CARDIAC IMAGING INTEGRATING E-SPECT WITH CT

In the process of SPECT image reconstruction, attenuation compensation plays a very important role in reducing artifacts. When attenuation compensation is applied to the human body, the best option is to use the patient-specific nonuniform attenuation map. There are two ways to obtain the attenuation map: one is through transmission, and the other is through non-transmission [18].

Among the non-transmission methods, one approach segmenting the lungs and outer body and then generating an attenuation map by assigning characteristic attenuation coefficients to the segmented regions [19]. A penalized least square algorithm was proposed by Kaplan for estimating

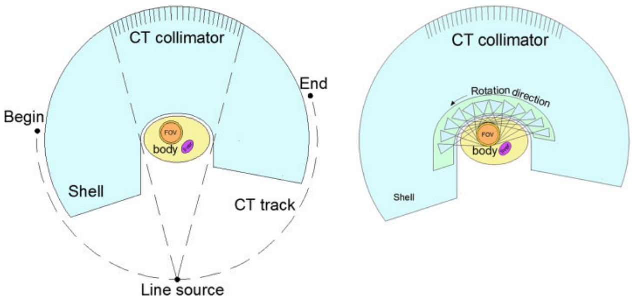

a) CT module b) SPECT module

FIGURE 7. **Scanner structure integrating E-SPECT with CT: a) shows imaging system with CT; b) shows imaging system with E-SPECT.**

activity and attenuation images from dual energy SPECT emission data [20]. The non-transmission methods approximate the attenuation map by assignment or iteration which is quite different from the real value.

The human attenuation map obtained by transmission method needs to use additional CT system [21], which is more accurate than non-transmission method [18]. Therefore, using the same machine to measure the attenuation map using CT method will be very effective for SPECT image reconstruction. The attenuation map can be obtained before or after the human body is scanned by SPECT. The CT system can be used not only to establish an attenuation mapping matrix, but also to provide important assistance for the precise positioning of the heart. For these reasons, the model proposed at the beginning has been improved to enable it to meet both CT and SPECT. Two conceptual drawings are used to describe the switch between the SPECT scan and CT scan, as shown in Fig.7.

Hybrid cardiac imaging integrating E-SPECT with CT can depict cardiac and vascular anatomical, and physiological information more accurately. The geometric structure of this proposed hybrid imaging system in Fig. 6 and Fig.7 is similar to that of an ellipse, and the geometric structure contains multiple detectors with slit-slat collimation, which utilizes the geometry of elliptical and multi-detectors to improve the sensitivity and signal to noise ratio (SNR), and incorporates a CT scanner into the system to obtain an accurate attenuation mapping matrix of the patient for image reconstruction. The conceptual diagram of Fig. 7(a) shows that the CT system has not been used at this time. At this point, the source of the x-ray can be shielded so that E-SPECT can be used to detect the human heart without worrying that the x-ray will contaminate the projection data.

When the CT system is needed, the x-ray source can be turned on, and the E-SPECT system is pulled down as a whole, so that the E-SPECT system is not in the position of the cross section of the heart to block x-rays, thereby ensuring the accuracy of the CT system to measure projection data. The overall structural concept diagram when using the CT system is shown in Fig.7(b). The E-SPECT system is already below the cross section of the heart, therefore this part of the structure is not shown.

The coverage angle of the two most peripheral rays that can be detected is slightly larger than the tangent angle of the line source to the ellipse, in which case the rays emitted by the line source cover the entire body contour of the person. During the detection process, the line source, the collimator and the detector make a circular motion around the human body. Finally, the transmission image of the human body can be obtained by using the Filtered Back Projection (FBP) or other algorithm, and then the attenuation mapping matrix corresponding to the human body can be derived.

C. IMAGE RECONSTRUCTION METHODS

There are many kinds of tomography reconstruction algorithms, which can be classified into two categories: one is iterative algorithm, another is analytical algorithm.

FBP is one of the most famous algorithms in analytical algorithms, and it is also one of the most widely used algorithms in commercial applications. It has the characteristics of fast and simple operation. However, FBP relies on filter operators to filter the signal, and the resolution will decrease after filtering. In addition, the traditional FBP algorithm does not consider the attenuation, noise, and scattering factors in the process of image reconstruction, which will lead to poor image quality. In 2000, NOVIKOV [22] proposed an image reconstruction algorithm under parallel projection and non-uniform attenuation. However, this algorithm still cannot complete the partial reconstruction of the image with complete projection data. Many related reconstruction algorithms [23], [24] have been proposed based Novikov's method, but they cannot effectively combine the physical effects of the model. In addition, the analytical algorithm has a big drawback: it is not possible to add some restrictive conditions arbitrarily. If some restrictive conditions need to be added, it will need to be re-derived, which will make the reconstruction algorithm more difficult.

The iterative algorithm is another kind of method for image reconstruction. It can add various constraints in the reconstruction process to improve the efficiency and accuracy of image reconstruction. The disadvantage of the iterative algorithm compared with the analytic algorithm is that the computation is more demanding and the operation time is relatively long.

Comparisons between analytical and iterative algorithms are made by using flat optical CT to illustrate the difference in computational complexity. Suppose an image has a size of 256×256 and a projection ray number of 128. It rotates at an increment of 2° and rotates a total of 180°. The number of projection rays is 11,520. According to the idea of analytic algorithm, these projection values are assigned to the image according to the projection direction, and then the image is filtered. All the computation here is to assign the values of 11,520 projection rays to the corresponding pixels. But the iteration algorithm does not use this idea. It obtains the projection value of the image by the value of the image before iteration, and then compares it with the real projection value. According to this comparison result, the value of each pixel of the image is repaired. The main calculation here is to update the image once with each ray, that is, the image needs to be updated 11,520 times. Because the iterative algorithm cannot complete the repair at one time, it needs to repeat the process many times until the required accuracy is satisfied. Therefore, the iterative algorithm needs more computation and time than the analytical algorithm. Bruyant also mentioned this in his paper [25].

However, the image reconstruction speed can be accelerated by using the projection map obtained by CT when initializing the image. With the development of science and technology, the CPU and GPU are running faster and faster. It is believed that the problem of slow computing speed will be solved in the near future. So an iterative method using the Ordered Subsets Expectation Maximization (OSEM) algorithm was developed for the image reconstruction of the integrating system.

1) ITERATIVE RECONSTRUCTION METHODS

Many studies have shown that the random noise in SPECT is Poisson distribution, and the radiation process of gamma photons satisfies the Poisson process. Image formation in SPECT can be described by the following expression [26].

$$\mathrm{Y} \sim \mathrm{Poisson}\,\{\mathbf{C}\mathrm{F}+\mathrm{R}\} \tag{4}$$

where, $\mathrm{Y}=[y_1, y_2, \ldots, y_M]^{\mathrm{T}}$ is the M×1 dimension vector that represents the measured projection data, and M represents the sum of the measured projection numbers. $\mathrm{F}=[f_1, f_2, \ldots, f_N]^{\mathrm{T}}$ is an N×1 vector representing an image vector, and N represents the sum of all pixel of the image. **C** is an M×N vector representing the response matrix of the system. $R = [r_1, r_2, \ldots, r_M]^{\mathrm{T}}$ is the $M\times 1$ vector representing the error caused by other factors, including noise and photon scattering. r_i represents the average error caused by the i$^{\mathrm{th}}$ ray detected by the detector.

From Eq.4, image reconstruction is an inverse problem to find F for a certain Y when response matrix C is known. We developed an iterative algorithm to reconstruct data acquired from an elliptical orbit. The point response function was derived for the projection operation. Considering E-SPECT with slit-slat collimation proposed in the paper, calibration is the process of estimating response matrix C for a particular scanner as accurately as possible for reconstructing images.

During cardiac SPECT detection, scattered photons cause artifacts in image reconstruction, reducing the contrast of the image. Since the scattered photon energy is lower than the normal photon energy, the energy window method is used here to eliminate the influence of scattered photons. The projection data of SPECT has random Poisson noise. It is difficult to filter it effectively by ordinary filter function. Here, Anscombe transform, also called square root transform, is used to convert Poisson noise in projection data into a Gaussian white noise. The noise is then filtered out of the projection data using a Wiener filter with a butterfly window based on the frequency domain characteristics of the projection data [27].

After the above steps, the confounding factors are considered to remove, and Eq.4 can be transformed into another description. The measured projection vector Y is Poisson distributed with expected value:

$$\mathrm{E(Y)} = \mathrm{CF} \tag{5}$$

Suppose we count along M lines, then the i$^{\mathrm{th}}$ element in the M dimensional projection vector, y_i, represents the total number of photons counted on the i$^{\mathrm{th}}$ ray collected during the data collection process. Therefore, the probability distribution of the total number of photons on the i$^{\mathrm{th}}$ ray can be written as:

$$P(y_i) = e^{-\lambda_i}\frac{\lambda_i^{y_i}}{y_i!} \tag{6}$$

where, λ_i represents the expectation value of the random variable y_i, which can be written as:

$$\lambda_i = \sum_{j=1}^{N} c_{ij} f_j \tag{7}$$

where, c_{ij} is the ij$^{\mathrm{th}}$ elements of the responds matrix A. c_{ij} indicating the probability that a photon is received from the pixel j by the detector i (the detector corresponding to the i$^{\mathrm{th}}$ ray). Then, the join distribution function of all projection data obtained from scanning, can be expressed as:

$$L(Y, F) = \prod_{i=1}^{M} e^{-c_{ij} f_j}\frac{(c_{ij}f_j)^{y_i}}{y_i!} \tag{8}$$

The likelihood function can be is processed by taking the logarithm of Eq.8:

$$\begin{aligned} L(Y, F) &= \sum_{i=1}^{M} (y_i \ln \lambda_i - \sum_{i=1}^{M} \ln y_i - \lambda_i) \\ &= \sum_{i=1}^{M} (y_i \ln \sum_{j=1}^{N} c_{ij} f_j - \sum_{j=1}^{N} c_{ij} f_j - \sum_{i=1}^{M} \ln y_i) \end{aligned} \tag{9}$$

The maximum likelihood function is used to calculate the value of vector F:

$$\frac{\partial ln L(Y, F)}{\partial f_j} = \sum\nolimits_{i=1}^{M} (-c_{ij} + \frac{c_{ij}\, y_i}{\sum_{j=1}^{N} c_{ij} f_j}) \tag{10}$$

Since the vector represented by F is very large, it is very difficult to solve it directly by solving the equation. Therefore, iterative solution is used to solve it. Here, the EM algorithm is used to iteratively solve the value of F. To solve the problem, the variable x_{ij} and its set X are introduced conveniently, x_{ij} represents the number of photons received by the detector i from the pixel j. x_{ij} obeys the independent Poisson distribution with a mean of $c_{ij} f_j$, so the actual projection value can be represented by Eq.11, which is substituted into Eq.9 to obtain a new likelihood function (Eq.12):

$$y_i = \sum_{j=1}^{N} x_{ij} \tag{11}$$

$$P = lnL(X, F) = \sum_{i=1}^{M}\sum_{j=1}^{N}(x_{ij}\ln(c_{ij}f_j) - c_{ij}f_j) \tag{12}$$

The EM algorithm is divided into two steps: step E (expectation value) and step M (expectation maximization).

Step E: obtain the expected value function $E\{\ln L(X|F)\}$.The random variable x_{ij} is an undetectable variable, so it is impossible to calculate $\ln L\ (X|F)$. By replacing the random variable x_{ij} with its expected value n_{ij}, calculating the expected value n_{ij} using the Bayes formula, and replacing the x_{ij} with the expectation value, a new likelihood function is obtained as follows.

$$n_{ij} = E(x_{ij}|y_i, F^{(k)}) = y_i \frac{c_{ij} f_j^{(k)}}{\sum_{j=1}^{N} c_{ij} f_j^{(k)}} \tag{13}$$

$$E(P|Y, F^{(k)}) = \sum_{i=1}^{M}\sum_{j=1}^{N}(n_{ij}\ln(c_{ij}f_j) - c_{ij}f_j) \tag{14}$$

Step M: Find the maximum value of the function $E(P|Y, F^{(k)})$ of the new target. The maximum value of function $E(P|Y, F^{(k)})$ can be found by taking the derivative with respect to f_j, i.e.,

$$\frac{\partial E(P|Y, F^{(k)})}{\partial f_j} = \sum_{i=1}^{M}(\frac{n_{ij}}{f_j} - c_{ij}) = 0 \tag{15}$$

By substituting Eq.13 in Eq.15, we can obtain:

$$f_j^{n+1} = \frac{f_j^n}{\sum_{l=1}^{M} c_{ij}} \sum_{i=1}^{M} c_{ij} \frac{y_i}{\sum_{l=1}^{N} c_{ij} f_l} \tag{16}$$

The maximum-likelihood expectation - maximization (ML-EM) algorithm converges slowly due to large amount of computation. The OS-EM algorithm is a modification of the ML-EM algorithm acting on different subset S_t of the projections. The projection data is divided into several subsets for computing. The standard way of dividing subsets in E-SPECT system is to take the projection data received by 12 slit-slat collimators per rotation as a subset, which can effectively speed up image reconstruction. This algorithm with a relaxation factor η_t can be rewritten as [28]:

$$f_j^{n+1} = f_j^n + \eta_t \frac{f_j^n}{\sum_{i=1}^{M} c_{ij}} \sum_{i \in S_t} c_{ij} \left[\frac{y_i}{\sum_{l=1}^{N} c_{il} f_l^n} - 1 \right] \tag{17}$$

The parameter f in Eq.17 can be initialized by the reconstructed image obtained by CT, and the projection data y can be divided into variable T ordered subsets so that there are different numbers of views in the subset for different iteration. Sheng proposed to optimize the OS-EM algorithm [28] using appropriate adjustment to ordered subsets to accelerate the convergence speed and improve the image quality.

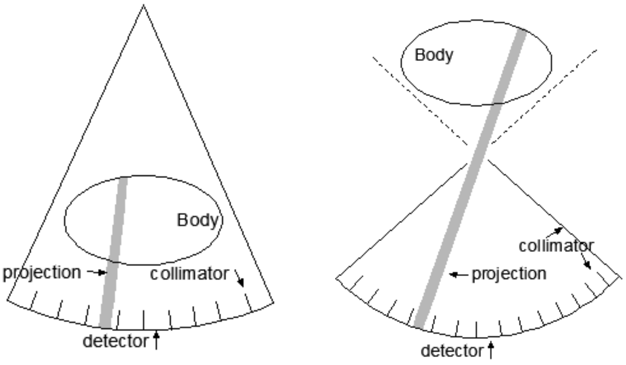

a) fan beam collimator b) slit-slat collimator

FIGURE 8. a) Shows fan beam collimators; b) shows slit-slat collimator system.

The proposed model appears different from the traditional model. However, there is no essential difference between this model and the traditional fan beam in terms of principle of reconstruction. The reconstruction equation is constructed by collecting the number of photon emission in a certain direction. The reconstruction is solving the equation E(Y) = CF for both models. The only difference here is that the specific values of the system matrix are different. The construction of the system matrix is related to the size of the specific device. The shape and size of the device affect the value of the system matrix but will not cause any changes in the formula of the reconstruction algorithm. Therefore, even in elliptical orbit, image reconstruction based on the above theory will not affect the reconstruction method. This model also proposes the use of multiple detectors, which is the same principle as the parallel beam projection with multiple detectors. It is equivalent to a detector collecting projection data at different locations. Therefore, this will not affect the reconstruction methods.

Semiconductor detectors and slit-slat collimators are mentioned in the model. Compared with traditional photomultiplier tubes, semiconductor detectors have better counting sensitivity and accuracy of photon emission. The accuracy of the measured values of projected rays changed in this part will make the measured values closer to the true values than before. And this part of the change will not change the form of the algorithm. The slit-slat collimator is different from the traditional fan-beam collimator. The differences are illustrated here using Fig.8.

It can be seen that the direction of receiving projection data is different, which changes the value of the corresponding system matrix. However, the algorithm itself is not changed, so the conclusion of the algorithm remains valid. The calculation method of the system matrix of this model is given below.

The only parameter missing is the system response matrix ***C***. The accuracy of the system response matrix affects the quality of the reconstructed image, and the system response matrix is a system specific characteristic that is independent of the human body. The acquisition of the system response matrix requires the determination of which model

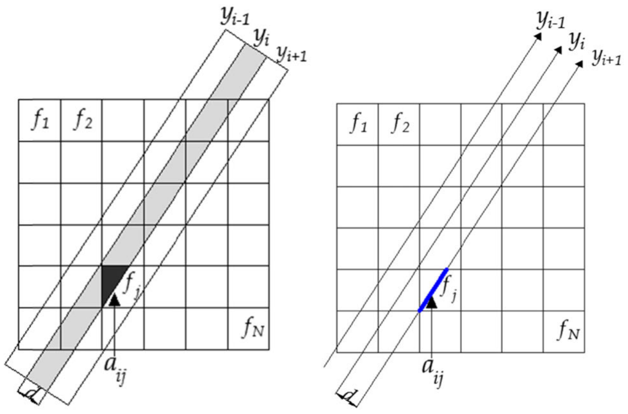

a) model 1 b) model 3

FIGURE 9. **Calculation model of the system response matrix; a) represents the system matrix of model 1; b) represents the system matrix of model 3.**

to use to describe the working process. Common projection matrix models can be divided into the following types:

Model 1: The projection ray is regarded as a beam of width d, and c_{ij} represents the area ratio of the area where the ith ray intersects the jth square Grid to the square grid, as shown in Fig. 9(a).

Model 2: The projection ray is regarded as a beam of width d, and the pixel value is concentrated at the center of the pixel. Whether the a_{ij} is 0 or 1 is determined according to whether the ith ray passes through the center of the jth pixel.

Model 3: The ray is regarded as a beam with a width of 0 and a spacing of d, and c_{ij} represents the length of the line intersecting the ith ray with the j pixel, as shown in Fig. 9(b).

The choice of the model is related to the accuracy of the system response matrix. Model 1 is computationally demanding, but the most accurate. The computation load of the second model is the smallest, but the reconstructed image is prone to noise, and the quality of the reconstruction is relatively poor. The calculation and precision of Model 3 are between Model 1 and Model 2. Considering that the computing power of modern computers will be greatly improved every 18 to 24 months, model 1 is used here to calculate the system response matrix.

The size of c_{ij} is related to the angle of incidence, the width and the incident position of the beam. In other words, after determining the equation of a ray, you can obtain the area of each grid covered by the ray and the area ratio (c_{ij}) to the square grid. Suppose that the motion trajectory of slit is $y = F(x)$ and that the ray angles of the outermost sides of the collimator that are allowed to enter are θ_1, θ_2, where θ_1, θ_2 ranges from $-180°$ to $180°$ and θ_2 is larger than θ_1.The width d of the ray is determined by the inherent resolution of the detector, so this parameter is known. Suppose a collimator can only accept n rays, so the angle θ_i of the ith ray is:

$$\theta_i = \begin{cases} \frac{\theta_1+\theta_2}{2} - arctan(\frac{n-2i}{n} * \tan\frac{\theta_2-\theta_1}{2}), & i \le \frac{n}{2} \\ \frac{\theta_1+\theta_2}{2} + arctan(\frac{2i-n}{n} * \tan\frac{\theta_2-\theta_1}{2}), & i > \frac{n}{2} \end{cases} \tag{18}$$

Assuming that the horizontal axis of the slit accepting the ith ray is x_i, and the ordinate is $y_i = F(x_i)$, the beam equation is:

$$y = (x - x_i)\tan\theta_i + y_i \tag{19}$$

After knowing the ray thickness d and ray equation, we can know the ratio of the area of each square intersected by the ray to the area of the square, so a_{ij} can be expressed by the following function:

$$a_{ij} = \delta(x_i, F(x_i), \theta_i, d, j) \tag{20}$$

2) IMAGE RECONSTRUCTION WITH COMPENSATION

The above formula is a reconstruction algorithm without attenuation correction. The algorithm should take attenuation correction into account to obtain a more accurate reconstructed image. Here we have an integrated CT system, and it is easy to obtain the attenuation map. When a ray passes through a homogeneous substance, its intensity decreases exponentially and its mathematical expression follows Lambert-Beer's law as shown in Eq. (21), where I represents the intensity of the ray after passing through the object, I_0 represents the intensity of the ray before passing through the object, u represents the linear attenuation coefficient of the substance, and l represents the length of the line through which the ray passes.

$$I = I_0 e^{-ul} \tag{21}$$

Using specific attenuation map from CT imaging, system response matrix with attenuation correction can be produced by the following equation:

$$a_{ij}(\mu) = c_{ij} e^{-\sum_{k\in L_{ij}} d_{ik}\times\mu_k} \tag{22}$$

where L denotes the set of pixels that photons pass through from pixel j to detector i, d_{ik} denotes the length of photons emitted by pixel i passing through pixel k, and $\mu_{\mathbf{k}}$ denotes the attenuation factor of pixel k. So the algorithm can be reformulated as:

$$f_j^{n+1} = f_j^n + \eta_k \frac{f_j^n}{\sum_{i=1}^{M} a_{ij}(\mu)} \sum_{i\in S_k} a_{ij}(\mu)\left[\frac{y_i}{\sum_{l=1}^{N} a_{il}(\mu) f_l^n} - 1\right] \tag{23}$$

3) RECONSTRUCTION FROM SEVERELY TRUNCATED DATA

Because the collimator segments focus on the central region, the geometric efficiency of E-SPECT proposed in this paper is increased greatly for this central high sensitivity region. However, the central region is severely truncated. E-SPECT/CT system acquires both CT and SPECT data. The CT image reconstructed can identify the contour of the truncated data to reconstruct the SPECT image. The truncation artifacts can be reduced by using the body contour as a support [29]. If the contour of body is known, we can use it as prior knowledge in the iterative reconstruction by setting the image pixels outside the support to zero. Images reconstructed with body contour as support has fewer artifacts than without support. E-SPECT with severely truncated data reconstructs images using the optimizing OS-EM algorithm with body contour as support to provide reasonably high count sensitivity, and temporal and spatial resolution.

Besides adding body contour constraints, we can also add other prior constraints to enhance the quality of image reconstruction. The total variation (TV) model proposed by Rudin *et al.* [30], is widely used in image denoising, restoration, reconstruction and other fields. The principle of the TV function is to regard the image as an energy system. The energy is minimal in the case of smooth and noiseless, so minimizing the total variation function is equivalent to minimizing the image energy, so as to obtain the optimal target image.

The TV function is the L1 norm of the image. The first-order property of the image has anisotropy and different diffusion characteristics for different image feature directions. Therefore, the image function edge method can preserve the image edge features well. It is better to smooth the area to be reconstructed. TV minimization regularization term is introduced in the reconstruction process. The reconstruction model with adding TV constraints and body contour constraints is represented by the following formula:

$$\begin{aligned} f &= arg\,min||f||_{TV} \\ &\quad st: P = C^{*}f, \quad f \geq 0, \ body(f) = 0 \end{aligned}$$

There are three constraints in this reconstruction model. The first one is the consistency constraint, which is used to ensure that the projected measurement of the reconstructed image is consistent with the actual one. The second is a non-negative constraint, which guarantees that there will be no negative in the image. The third is the body contour constraint used to ensure that pixels outside the body are zero.

It is difficult to directly find the minimum value of the TV function, so the gradient descent algorithm is used to solve the problem. The adaptive step size ASD-POCS algorithm framework can easily obtain the minimum TV value of the image. Therefore, we propose an algorithm based on ASD-POCS [11] and OSEM as the core.

The specific algorithm is as follows:

```
1. The CT image is reconstructed by the FBP algorithm to obtain the human body attenuation map.
2. Initialize the image $f$ according to the contour of the CT image. The pixels outside the contour are set to 0, and the pixels in the contour are set to 1.
3. $\beta = 1.0$, $\beta$ red $= 0.995$, ng $= 20$, $\alpha = 0.2$
4. rmax $= 0.95$, $\alpha$ red $= 0.95$.
5. For  i = 1: irt_num    //Start the main loop
6.    for  j=1:$S_k$  //Start the ordered subset loop
7.  $f_0 = f$
8.       using the attenuation corrected OSEM algorithm
     $f_j^{n+1} = f_j^n + \eta_k \frac{f_j^n}{\sum_{i=1}^{M} a_{ij}(u)} \sum_{i \in S_k} a_{ij}(u) \left[ \frac{y_i}{\sum_{i=1}^{M} a_{il}(u) f_l^n} - 1 \right]$
9.     $f \geq 0$
10. $f\_ROI$= extract the region of interest.
11. $g = af \ \ dd = |g - g_0|$
12. $dp = |f - f_0|$
13. if {first iteration} then $dtvg = \alpha^{*}\ dp$
14.  $f_0 = f$
15.    for i = 1: $ng$
16.     $df = \nabla_f ||f||_{TV}$
17.      $df = df/|df| \quad f = f - dtvg^{*}df$
18. end
19. $dg = |f - f_0|$
20. If  dg > rmax * $dp$ and $dd > \in$
21.   $dtvg = dtvg\ ^{*}\alpha$ red
22. $\beta = \beta^{*}\beta$ red
23. $f$ = Covering the region of interest of $f$ with $f\_ROI$
24. end          //end ordered subset loop
25. Set the Outside Pixel of Body Contour to 0
26. end             //end main loops
27. Return $f$
```

Symbol // indicates a comment description. The parameters in steps 3 and 4 of the algorithm are used to control the step size of gradient descent. The 8th step of the algorithm represents the data consistency constraint, and the OSEM algorithm with attenuation correction is used. Step 9 of the algorithm is used to ensure the non-negativity of the image. Step 10 indicates that the region of interest is extracted in order to prevent excessive smoothing. Steps 11 to 13 are used to calculate the initial step size. Steps 16 and 17 of the algorithm use the gradient descent algorithm to minimize the TV of the image. The variable *ng* is used to control the number of TV. If *ng* is too large or too small, it will affect the results. Steps 19 through 22 of the algorithm are used to control the step size of the gradient descent. In the 23 step of the algorithm, the region of interest extracted from the 10th step is covered and fused. Step 25 of the algorithm is used to ensure that during the iteration process, no more than 0 pixels will appear on the periphery of the body contour.

III. SIMULATION

A quality assurance Phantom was designed and reconstructed to assess the performance of cardiac imaging integrating SPECT and CT proposed in this paper. The generation of simulation data here does not add the noise to ensure that the focus of attention is on the accuracy of image reconstruction using attenuated truncated projection data. The cardiac phantom is shown in Fig.10.

In Fig.10, the large ellipse can be regarded as a human body with a long axis radius of 200 mm, a short axis radius of 140 mm, and a density of 30%. This model can represent the contours of most people. The small ellipse has a long axis radius of 45 mm, a short axis radius of 29 mm, and a density of 50%, indicating the lungs of the human body, which affects image reconstruction. The circle in the middle represents the heart of the human body, with a radius of 70 mm, an outer contour density of 100%, and an inner density of 30%. In the middle of the circle there are four groups of 12 dots, each of which has a diameter of 3, 5, 7 and 9 mm, with a density

FIGURE 10. Cardiac phantom.

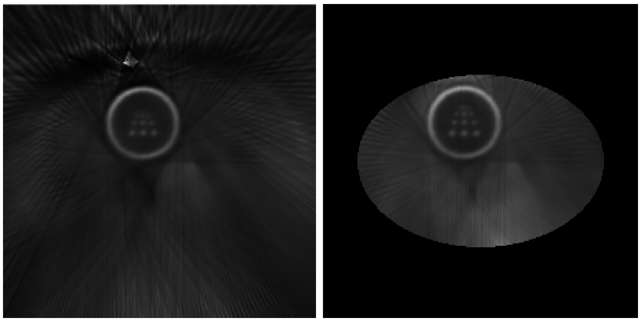

a) without body contour support b) with body contour support

FIGURE 11. a) Shows the image reconstructed without body contour support; b) shows the image reconstructed with body contour support.

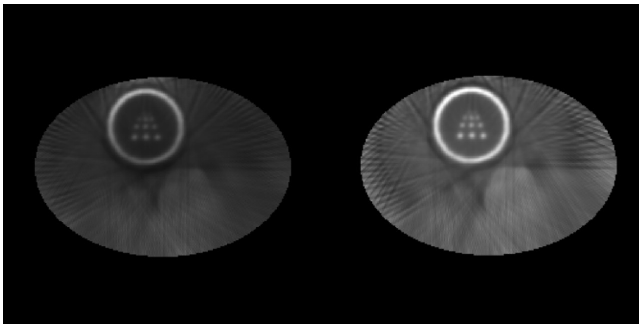

(a) (b)

FIGURE 12. The image reconstructed without attenuation correction (a) and the image reconstructed with attenuation correction (b).

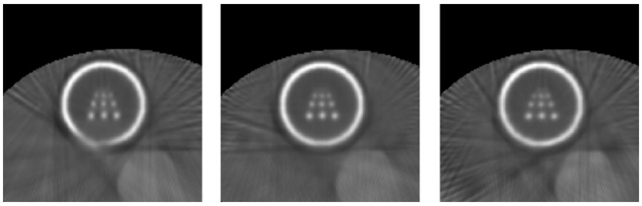

(a) 180° (b) 210° (c) 240°

FIGURE 13. Reconstruction results under different coverage angles.

of 100%. The distance between the dots is the sum of their diameters. These dots are set here to examine the resolution of the image. The sampling angle in the image reconstruction process must be greater than or equal to 180° to have a better reconstruction effect, so the sampling angles we use here are 180°, 210°, and 240°, respectively.

One advantage of the iterative algorithm over the analytical algorithm is that various constraint conditions can be added to the iterative process to make the reconstruction more accurate. Therefore, the constraint condition of body contour information is added to the process of iterative reconstruction. Fig.11 (a) and (b) show the results of iterative reconstruction with and without volume contour constraints without any additional constraints.

In Fig.10, it is obvious that there are serious artifacts on the edge when the body contour restriction information is not added. After adding the restriction conditions, the artifacts on the edge are reduced and the imaging is closer to the real situation of the human body. Adding prior knowledge of body contours is reflected in steps 2 and 25 of the proposed algorithm.

In the SPECT reconstruction algorithm, attenuation correction is one of the most important aspects [12]. If the attenuation correction of projection data is not carried out in the reconstruction process, the reconstruction results will be seriously deviated. In order to verify this point of view, the body contour constraint is added on the basis of the standard OSEM algorithm but the attenuation correction is not performed, and the reconstruction result is shown in Fig. 12. From the reconstruction results, it can be seen that the region of interest has produced serious signal drop. Therefore, attenuation correction is added to the algorithm. In the first step of the algorithm, attenuation map is obtained by the CT image, and in the eighth step, attenuation correction is added to the OSEM reconstruction process.

Sampling coverage angle is also a factor that affects the quality of reconstructed image. In general, the larger the sampling coverage angle, the better the quality of reconstructed image. Because the system needs to be compatible with CT system, in order to obtain a good SNR, the human body and the detector need to be as close as possible, so it cannot achieve 360° full sampling coverage angle. Images reconstructed with the sampling angles of 180°, 210°, and 240° are simulated, and results are shown in a, b, and c in Fig.13, respectively.

When performing a simulated reconstruction, the value of the coverage angle is determined by the first detector at the beginning and the last detector at the end. The starting angle is set to 0° in the simulation, and the angle of the last detector at the end of the simulation is the set coverage angle.

The detectors rotate during the imaging process at a 3° and the total range is 15°, which means there are 6 sets of projection values. The angle of the last detector before rotation is subtracted from the coverage angle by 15 degrees, which is used to distribute the angle evenly to each detector in the simulation reconstruction process. Then the simulator rotates to collect the projection values at various angles, so that 72 projection values can be obtained for image reconstruction.

TABLE 2. Deviation at different coverage angles.

	Fig.13(a)	Fig.13(b)	Fig.13(c)
NMSD	0.599	0.553	0.573
NAAD	0.070	0.064	0.068
WCCD	0.550	0.528	0.513

It can be clearly seen from Fig.13(a) that there is a significant artifact in the bottom of the edge at the 180° sampling coverage angle.

The reconstructed quality of the FOV regions of (b) and (c) in Fig.13 is much better than that of (a), but the difference between (b) and (c) in the FOV region is not substantial under the naked eye. Therefore, it is necessary to quantitatively characterize the reconstructed quality of (b) and (c). Here we use three indicators to compare the difference between the reconstructed image and the original image.

1. Normalized mean square distance criterion (NMSD):

$$NMSD = \left[\frac{\sum_{u=1}^{M}\sum_{v=1}^{N}(t_{u,v}-r_{u,v})^2}{\sum_{u=1}^{M}\sum_{v=1}^{N}(t_{u,v}-t_{avg})^2}\right]^{\frac{1}{2}} \tag{24}$$

2. Normalized mean absolute distance criterion (NAAD):

$$NAAD = \frac{\sum_{u=1}^{M}\sum_{v=1}^{N}\left|t_{u,v}-r_{u,v}\right|}{\sum_{u=1}^{M}\sum_{v=1}^{N}\left|t_{u,v}\right|} \tag{25}$$

3. Worst case criterion distance (WCCD):

$$\begin{aligned} WCCD &= \max_{\substack{1\le i\le[M/2]\\1\le j\le[N/2]}} |T_{ij}-R_{ij}| \\ T_{ij} &= \frac{1}{4}(t_{2i,2j}+t_{2i+1,2j}+t_{2i,2j+1}+t_{2i+1,2j+1}); \\ R_{ij} &= \frac{1}{4}(r_{2i,2j}+r_{2i+1,2j}+r_{2i,2j+1}+r_{2i+1,2j+1}) \end{aligned} \tag{26}$$

In these three formulae, t, r represent the original image and the reconstructed image, respectively, u, v represents the subscript of the image, the image size is $M\times N$, t_{avg} represents the average value of the image, the indicators of each image in Fig. 11 are shown in Table 2.

The above three indicators reflect the performance of different aspects of the reconstruction algorithm. The index NMSD is more sensitive to pixels with larger errors in the image. Index NAAD is more sensitive to small errors in many pixels, and index WCCD mainly reflects the maximum difference between the reconstructed image and the original image.

According to the theory of reconstruction algorithm, the projection angle of at least 180° is needed when using parallel beam for reconstruction. Based on the reconstruction theory of parallel beam, it can be inferred that the projection angle of fan beam projection is at least $180° + \beta$ (the angle of fan beam). In the proposed model, detectors connected by slit-slat collimators can be regarded as a fan beam, so the projection angle needed is at least $180° + \beta$. It is undeniable that the bigger the projection angle is, the information that the data can bring is more complete. However, if the projection angle is enlarged, the obese population will not be suitable. If the size of the machine is enlarged to adapt to the crowd, the distance between the detector and the target will be enlarged, and the SNR will be reduced. Therefore, it is necessary to choose a suitable coverage angle to deal with the above problems in the model design.

The process of collecting projection data of the model proposed in this paper is essentially the same as the fan beam projection. In this model, the value of angle β is largely determined by angle α between the edges of the two slit-slats (see Table 1), and the angle has been enlarged for angle α in order to ensure full coverage of the FOV region. The actual required β is smaller than angle α of the two, and angle β should be around 30°. For this reason, we added a 210° coverage angle for the simulation reconstruction. In the reconstructed image of Fig. 13, it is obvious that there are artifacts at the bottom of the reconstructed image at 180°, and the artifacts disappear at 210° which indicates that the coverage angle at this time has reached $180° + \beta$. In order to observe reconstruction results larger than 210°, we use 240° coverage angle. At this time, there is no artifact in the reconstruction results.

It can be clearly seen from Table 2 that the values of each index of the reconstructed image at system coverage angles of 210° and 240° are better than those of the reconstructed image with a coverage angle of 180°.The NAAD and NMSD of the reconstruction image with a system coverage angle of 210° are better than the reconstruction with a system coverage angle of 240°, but the WCCD is relatively poor. However, comparing table 3, we can find that the NAAD parameters are not consistent with the parameters in table 2. This is because the TV constraints affect the parameters. The larger the coverage angle in the model, the farther the end detector is from the human heart. This will cause the SNR of a part of the data to be greatly reduced, resulting in poor reconstruction quality. Considering the SNR and other hardware aspects of the model system, we propose that the coverage angle of the system should be a value between 210 and 240 on the premise of guaranteeing the quality of image reconstruction and balancing the performance of the proposed three parameters.

In order to prove that adding the TV constraint in the reconstruction process is beneficial to reduce the deviation of the region of interest (ROI) of the reconstructed image, We respectively present reconstructed images with TV constraint terms at sampling angles of 180°, 210° and 240°.The reconstructed image is shown in Fig.14. In order to quantify the reconstruction quality, the indicators of the ROI with TV are given, as shown in Table 3. Comparing the data in Table 2 with the data in Table 3, it can be clearly seen that under each coverage angle, the quality of reconstructed images after TV minimization is better than the quality of reconstructed images without TV minimization.

Now we present the reconstructed image obtained by the standard OSEM algorithm without any constraints and

TABLE 3. Deviation at different coverage angles.

	Fig.14(a)	Fig.14(b)	Fig.14(c)
NMSD	0.565	0.527	0.533
NAAD	0.043	0.039	0.035
WCCD	0.521	0.513	0.508

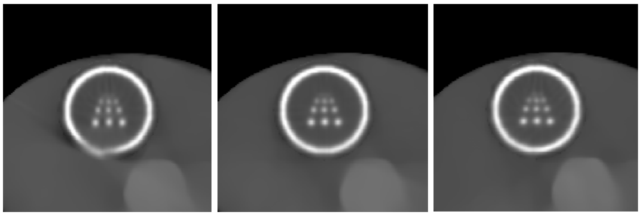
(a)180° (b)210° (c)240°

FIGURE 14. Reconstruction results with TV constraint.

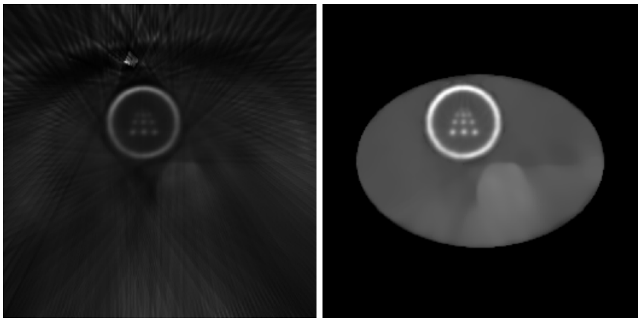
a) Standard OSEM (b) Proposed algorithm

FIGURE 15. Image reconstructed with standard OSEM is shown in a); image reconstructed with proposed algorithm is shown in b).

the reconstructed image obtained by using our proposed algorithm, as shown in Fig.15. For these two reconstructed images, even the naked eyes can tell the difference easily. We can draw a conclusion that using our proposed reconstruction algorithm on our SPECT model can achieve better reconstruction results than using standard OSEM algorithm.

There are four sets of dots with different sizes in the original image. The diameter of each group of dots is 3, 5, 7 and 9 mm, respectively. It can be observed that three sets of dots in the reconstructed image can be clearly resolved. The dots with a diameter of 3 mm cannot be resolved but the set of dots with a diameter of 5 mm can be resolved. This is consistent with the fact that the spatial resolution of the model obtained by Eq.1 is 4.9 mm.

The number of iterations is also an important parameter that affects the quality of reconstructed images. Therefore, the quality of the reconstructed image is tested by varying the number of iterations at system coverage angle of 240°. Fig.16 shows the trends of the NMSD, NAAD, and WCCD under different iterations. The image reconstruction quality becomes better as the number of iterations increases using our proposed reconstruction algorithm but there is no significant improvement after the number of iteration is greater than 5. Considering the time and image quality, the number of iterations of reconstructed images should be between 5 and 6 times.

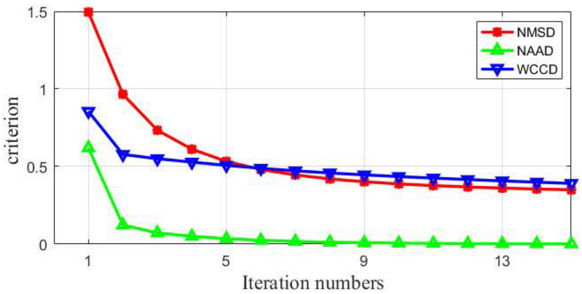

FIGURE 16. Deviation with different iterations.

IV. CONCLUSION

We propose a novel E-SPECT system with slit-slat collimator that can effectively improve the efficiency and sensitivity of the system. The E-SPECT for cardiac imaging can significantly increase the geometric efficiency for the central region, which is about two times higher than that of the dual-head SPECT system. The system is integrated with CT, which can quickly locate the organ to be detected before SPECT detection and provide accurate attenuation mapping matrix for image reconstruction. We also propose a new algorithm based on ASD-POCS and OSEM for the image reconstruction of this new system. The artifacts and distortions associated with small FOV cardiac imaging can be substantially suppressed by using the proposed reconstruction algorithm and compensation methods. The simulation experiment shows that by using the proposed algorithm and adding some constraints such as body contours, the quality of the reconstructed image is greatly improved. We find that the sampling coverage angle is optimal from 210° to 240° in this model, and the number of iterations is 5 to 6. Further development of cardiac SPECT imaging depends largely upon the collimator design and detector modules, and reconstruction algorithms.

REFERENCES

[1] S. S. Gambhir, D. S. Berman, J. Ziffer, M. Nagler, M. Sandler, J. Patton, B. Hutton, T. Sharir, S. Ben Haim, and S. B. Haim, "A novel high-sensitivity rapid-acquisition single-photon cardiac imaging camera," *J. Nucl. Med.*, vol. 50, no. 4, pp. 635–643, 2009.

[2] A. Celler, T. Farncombe, C. Bever, D. Noll, J. Maeght, R. Harrop, and D. Lyster, "Performance of the dynamic single photon emission computed tomography (dSPECT) method for decreasing or increasing activity changes," *Phys. Med. Biol.*, vol. 45, no. 12, pp. 3525–3543, 2000.

[3] D. L. Bailey and K. P. Willowson, "Anevidence-based review of quantitative SPECT imaging and potential clinical applications," *J. Nucl. Med.*, vol. 54, no. 1, pp. 83–89, 2013.

[4] C. Liu, J. Xu, and B. M. Tsui, "Myocardial perfusion SPECT using a rotating multi-segment slant-hole collimator," *Med. Phys.*, vol. 37, no. 4, p. 1610, 2010.

[5] D. Hwang, G. L. Zeng, "Reduction of noise amplification in SPECT using smaller detector bin size," *IEEE Trans. Nucl. Sci.*, vol. 52, no. 5, pp. 1417–1427, Oct. 2005.

[6] M. T. Madsen, "Recent advances in SPECT imaging," *J. Nucl. Med.*, vol. 48, no. 4, pp. 661–673, 2007.

[7] J. A. Patton, P. J. Jaslomka, G. Germano, and D. S. Berman, "Recent technologic advances in nuclear cardiology," *J. Nucl. Cardiol.*, vol. 14, no. 4, pp. 501–513, 2007.

[8] S. C. Blankespoor, X. Xu, K. Kaiki, J. K. Brown, H. R. Tang, C. E. Cann, and B. H. Hasegawa, "Attenuation correction of SPECT using X-ray CT on an emission-transmission CT system: Myocardial perfusion assessment," *IEEE Trans. Nucl. Sci.*, vol. 43, no. 4, pp. 2263–2274, Aug. 1996.

[9] A. K. Buck, S. Nekolla, S. Ziegler, A. Beer, B. J. Krause, K. Herrmann, K. Scheidhauer, H. J. Wester, E. J. Rummeny, M. Schwaiger, and A. Drzezga, "SPECT/CT," *J. Nucl. Med.*, vol. 49, no. 8, pp. 1305–1319, 2008.

[10] S. Scharf, "SPECT/CT imaging in general orthopedic practice," *Seminars Nucl. Med.*, vol. 39, no. 5, pp. 293–307, 2009.

[11] R. J. Jaszczak, "The early years of single photon emission computed tomography (SPECT): An anthology of selected reminiscences," *Phys. Med. Biol.*, vol. 51, no. 6, pp. 99–115, 2006.

[12] Y. Sheng and J. Sheng, "A cardiac SPECT system with multiple collimated detectors rotating in an elliptical orbit," *J. Comput. Eng. Inf. Technol.*, vol. 5, no. 3, pp. 1–5, 2016.

[13] J. Sheng, "An elliptical SPECT system with slit-slat collimation for cardiac imaging," *Comput. Med. Imag. Graph.*, vol. 35, no. 1, pp. 9–15, 2011.

[14] G. L. Zheng and D. Gagnon, "CdZnTe strip detector SPECT imaging with a slit collimator," *Phys. Med. Biol.*, vol. 49, no. 11, pp. 2257–2271, 2004.

[15] H. O. Anger, "Radioisotope cameras," in *Instrumentation in Nuclear Medicine*, vol. 1, G. J. Hine, Ed. New York, NY, USA: Academic, 1967, pp. 485–552.

[16] R. Accorsi, J. R. Novak, A. S. Ayan, and S. D. Metzler, "Derivation and validation of a sensitivity formula for slit-slat collimation," *IEEE Trans. Med. Imag.*, vol. 27, no. 5, pp. 709–722, May 2008.

[17] Y. H. Kao and N. Better, "D-SPECT: New technology, old tricks," *J. Nucl. Cardiol.*, vol. 23, pp. 311–312, Apr. 2016.

[18] A. Krol, J. E. Bowsher, S. H. Manglos, D. H. Feiglin, M. P. Tornai, and F. D. Thomas, "An EM algorithm for estimating SPECT emission and transmission parameters from emission data only," *IEEE Trans. Med. Imag.*, vol. 20, no. 3, pp. 218–232, Mar. 2001.

[19] M. T. Madsen, P. T. Kirchner, J. P. Edlin, M. A. Nathan, and D. Kahn, "An emission-based technique for obtaining attenuation correction data for myocardial SPECT studies," *Nucl. Med. Commun.*, vol. 14, no. 8, pp. 689–695, 1993.

[20] M. S. Kaplan, D. R. Haynor, and H. Vija, "A differential attenuation method for simultaneous estimation of SPECT activity and attenuation distributions," *IEEE Trans. Nucl. Sci.*, vol. 46, no. 3, pp. 535–541, Jun. 1999.

[21] B. H. Hasegawa, T. F. Lang, J. K. Brown, E. L. Gingold, S. M. Reilly, S. C. Blankespoor, S. C. Liew, B. M. W. Tsui, and C. Ramanathan, "Object-specific attenuation correction of SPECT with correlated dual-energy X-ray CT," *IEEE Trans. Nucl. Sci.*, vol. 40, no. 4, pp. 1242–1252, Aug. 1993.

[22] R. G. Novikov, "An inversion formula for the attenuated X-ray transformation," *Arkiv Matematik*, vol. 40, no. 1, pp. 145–167, 2002.

[23] L. A. Kunyansky, "A new SPECT reconstruction algorithm based on the Novikov explicit inversion formula," *Inverse Problems*, vol. 17, no. 2, p. 293, 2001.

[24] J. Wen, T. Li, and Z. Liang, "Ray-driven analytical fan-beam SPECT reconstruction with nonuniform attenuation," in *Proc. ISBI*, 2002, pp. 629–632.

[25] P. P. Bruyant, "Analytic and iterative reconstruction algorithms in SPECT," *J. Nucl. Med.*, vol. 43, no. 10, pp. 1343–1358, 2002.

[26] K. Lange and R. Carson, "EM reconstruction algorithms for emission and transmission tomography," *J. Comput. Assist. Tomogr.*, vol. 8, no. 2, pp. 306–316, 1984.

[27] J. H. Cheng "Frequency-domain approaches to quantitative brain SPECT," Ph.D. dissertation, State Univ. New York Stony Brook, Stony Brook, NY, USA, Dec. 1997.

[28] J. Sheng and D. Liu, "An improved maximum likelihood approach to image reconstruction using ordered subsets and data subdivisions," *IEEE Trans. Nucl. Sci.*, vol. 51, no. 1, pp. 130–135, Feb. 2004.

[29] S. H. Manglos, "Truncation artifact suppression in cone beam radionuclide transmission CT using maximum likelihood techniques: Evaluation with human subjects," *Phys. Med. Biol.*, vol. 37, no. 3, pp. 549–562, 1992.

[30] L. I. Rudin, S. Osher, and E. Fatemi, "Nonlinear total variation based noise removal algorithms," in *Proc. 11th Int. Conf. Center Nonlinear Stud. Exp. Math., Comput. Issues Nonlinear Sci.*, 1992, pp. 256–268.

JINHUA SHENG (SM'06) received the Ph.D. degree in nuclear electronics from the University of Science and Technology of China, in 1997.

He had 16 years of experience as a Postdoctoral Research Fellow, a Research Scientist, a Research Associate, a Research Fellow and Faculty, at prominent institutions of the USA, including the University of Illinois, the University of Wisconsin, the University of Missouri, and Indiana University. He previously served as an Associate Professor and the Associate Dean of the Graduate School, China Academy of Telecommunications Technology. As a Researcher and an Expert in image processing, medical imaging science, and neuroscience, he has contributed a lot in his area of specialization. From April 2005 to December 2008, he was a Postdoctoral Research Fellow with the University of Wisconsin, USA. He is currently a Distinguished Professor with Hangzhou Dianzi University, China, and the Director of the Key Laboratory of Intelligent Image Analysis for Sensory and Cognitive Health, Ministry of Industry and Information Technology of China, Hangzhou, Zhejiang, China. He has published over 60 research articles in some top journals and international conferences, such as *Science Translational Medicine*, the IEEE TRANSACTIONS ON COMPUTATIONAL BIOLOGY AND BIOINFORMATICS, the IEEE TRANSACTIONS ON NUCLEAR SCIENCE, the IEEE TRANSACTIONS ON MEDICAL IMAGING, *Magnetic Resonance in Medicine*, *Neuroimaging*, and *Behavioural Brain Research*, and been granted one U.S. patent. His research works have been reported in some professional media, such as Science Daily and First Science. He is an active reviewer for many peer-reviewed journals and some top international conferences. He served as the Chief Editor for one journal in China and served as an Editor for four journals in the USA.

YANGJIE MA received the bachelor's degree from the Zhejiang University of Technology, China, in 2016. He is currently pursuing the master's degree in computer science with Hangzhou Dianzi University, China. His research interests include low-dose CT imaging, biosignal processing, and single photon imaging technology.

WEIXIANG LIU is currently pursuing the master's degree in computer science with Hangzhou Dianzi University, China. Her research interests include medical imaging, image reconstruction, and machine learning.

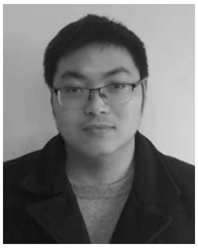

QINGQIANG LIU received the bachelor's degree in information and computing science from the Shangqiu Normal College, Shangqiu, Henan, China, in 2016. He is currently pursuing the master's degree in computer science with Hangzhou Dianzi University. His research interests include medical imaging, brain networks analysis, and machine learning.

• • •